Improvements to the AERIoe Thermodynamic Profile Retrieval Algorithm

David D. Turner ⃝ and W. Greg Blumberg ⃝

Abstract—Temperature and humidity profiles in the atmospheric boundary layer (i.e., from the surface to 3 km) can be retrieved from ground-based spectral infrared observations made by the atmospheric emitted radiance interferometer (AERI) at high temporal and moderate vertical resolution. However, the retrieval is an ill-posed problem, and thus there are multiple thermodynamic solutions that might satisfy the observed radiances. Previous work developed a physical-iterative method called AERIoe that retrieved temperature and water vapor mixing ratio profiles from these radiance observations in both clear and cloudy conditions. The AERIoe algorithm was modified to enforce two physical constraints, namely that the derived relative humidity must be less than 100% and that the potential temperature must be monotonically increasing with height above some thin potentially subadiabatic layer after each iteration. Furthermore, additional observations including *in situ* surface meteorology, numerical weather prediction model output, microwave brightness temperatures, and partial profiles of water vapor from a Raman lidar were incorporated into the observation vector of the retrieval along with the infrared radiance observations. The addition of these new observations markedly improved the accuracy of the temperature profiles, especially above 2 km, and the water vapor profiles relative to radiosondes. These improvements are seen using cases from the tropics, mid-latitudes, and Arctic.

Index Terms—Atmospheric measurements, infrared radiometry, remote sensing.

I. INTRODUCTION

THERMODYNAMIC profiles in the atmospheric boundary layer (i.e., the lowest 3 km of the troposphere) are essential for a wide range of applications, including hazardous weather nowcasts and forecasts, initialization of numerical weather prediction (NWP) models, aviation safety applications such as fog prediction, pollution dispersion modeling, and wind energy forecasts. Experts in all of these areas desire a higher temporal resolution (order of 15 min or better) and vertical resolution (order

of 100 m just above the surface) for their applications. Indeed, a large number of reports have consistently called for the need for a thermodynamic profiling network composed of ground-based remote sensors (e.g., [1]–[4]). While there are several potential technologies that are able to provide these observations (e.g., [5] and [6]), only a few of them are currently available commercially.

One of these sensors is the atmospheric emitted radiance interferometer (AERI). The AERI is a ground-based infrared spectrometer that passively observes radiance emitted by the atmosphere. AERI radiance observations have been used in a wide range of scientific applications including cloud remote sensing (e.g., [7]–[10]), improving infrared radiative transfer models (e.g., [11] and [12]), characterization of dust properties in the troposphere [13], trace gas retrievals [14], and quantification of radiative forcing by trace gases [15]. However, it was recognized early in its development history that the AERI observations were sensitive to the evolution of the thermodynamic profile in the boundary layer, and a physical-iterative retrieval method was developed to invert these radiance observations to get the profiles [16], [17]. This algorithm, henceforth called AERIprof, was used to look at the evolution of the stability and convective nature of the atmosphere (e.g., [18]–[20]).

AERIprof had several limitations. First, it used a fixed carbon dioxide (CO_2) concentration profile (at 360 ppm) that was not easily changed. This created a problem on two time scales: the seasonal variability of the CO_2 could not be captured nor could the annual increase in the CO_2, and both of these resulted in biases in the temperature and humidity profile. Second, physical retrievals require a first guess solution, and the AERIprof algorithm was very dependent on the accuracy of this first guess; if the first guess was poor, then the retrieval would not converge. Third, as downwelling infrared radiance is very sensitive to small changes in cloud properties like liquid water path (e.g., [10]), and it is difficult to accurately estimate the needed cloud properties using other sensors, AERIprof often did not converge to a solution in most cloudy situations. Fourth, the AERIprof algorithm did not provide uncertainty estimates for the retrieved thermodynamic profiles, making the results difficult to properly use in any data assimilation scheme. Lastly, AERIprof used a statistically-based forward model that was optimized for the Southern Great Plains, effectively limiting the geographical regions that could be processed using this algorithm.

To overcome these limitations, a new physical-iterative retrieval based upon a Gauss–Newton optimal estimation scheme was developed [21]. This new algorithm, henceforth called
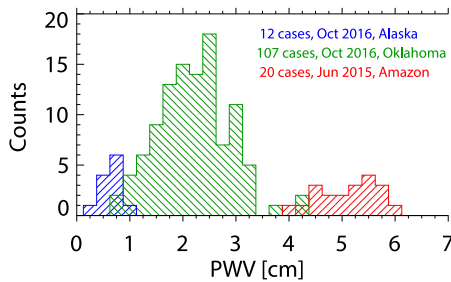
Fig. 1. Distribution of PWV from the three sites used in the baseline comparison of the v1 and v2 versions of AERIoe.

AERIoe, is capable of retrieving thermodynamic profiles in both clear and cloudy conditions, converging over 95% of the time. This paper discusses how the original AERIoe algorithm has been extended to include other observational datasets in the retrieval, and demonstrates their impact on the accuracy and uncertainty of the retrieved profiles. In addition, we also demonstrate the ability of AERIoe to retrieve temperature and humidity in various climatic regimes.

II. DATA SOURCES

This study uses datasets that were collected as part of the Department of Energy's Atmospheric Radiation Measurement (ARM) program [22]. In particular, we will use data collected at the ARM Southern Great Plains (SGP; 36.61°N, 97.49°W) site in north-central Oklahoma [23] and by the ARM Mobile Facilities [24] in both Oliktok, Alaska (70.50°N, 149.88°W) and near Manaus, Amazon (−3.21°N, 60.60°W). These data, collected in October 2016 for the SGP and Oliktok datasets and June 2015 for the Amazon dataset, span a large range of precipitable water values (PWV; see Fig. 1).

A. AERI

The AERI is a hardened automated infrared spectrometer that was built for the ARM program by the Space Science and Engineering Center at the University of Wisconsin – Madison [25], [26]. The engineering of the AERI system has allowed the ARM program to deploy it at all of its main facilities, including the SGP and in the Arctic and Tropics. Its original purpose was to provide the accurate spectral infrared radiance data needed to improve infrared line-by-line radiative transfer models (LBLRTMs) [27] that serve as the basis for faster radiation parameterizations used in climate models [28].

The radiometric calibration, which is achieved by accounting for the nonlinearity of the detectors and by regularly observing two well-characterized NIST-traceable blackbody targets that are maintained at different temperatures, is better than 1% of the ambient radiance (this is a 3-σ estimate) [29]. Additionally, the spectral calibration is approximately 1.5 ppm (1−σ) [29]; this is important for atmospheric profiling which is highly dependent on the locations, strengths, and widths of the atmospheric absorption lines.

The temporal resolution of the AERI radiance observations is approximately 20 s. The AERIs were modified from the
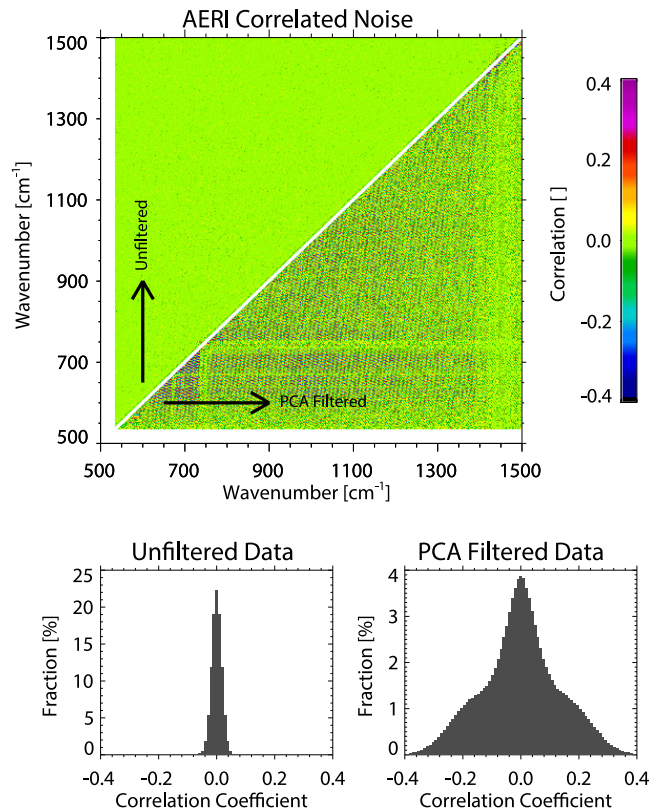

Fig. 2. AERI observation covariance matrix, expressed as a correlation matrix, determined from a long-time series observation of a blackbody in the zenith port. Since the matrix is symmetric, one half of the matrix shows the correlation from the unfiltered data, whereas the other half shows the correlation after applying the noise filter. The two histograms show the distribution of the correlation values from each half.

original 7 min resolution to this "rapid-sample" resolution in 2004–2005 to facilitate cloud property studies, as cloud properties often change dramatically as the clouds advect across the AERI's 46 mrad field-of-view [30]. However, this rapid-sampling greatly increases the random error in the radiance observations. To reduce the noise level, a principal component (PC) based noise filter is applied to the AERI radiance observations; this filtering reduces the random noise level to approximately the same level as the 7 min data [30]. Note that this noise filter uses an objective method to determine how many PCs to use in the reconstruction; approximately 340 PCs were used for both the SGP and Amazon sites and 175 PCs for the Oliktok site. The reduction in the magnitude of the noise was confirmed via long stares at a blackbody in the zenith port (see Fig. 2). While the noise filtering does result in some channel-to-channel correlation, the absolute values of these correlations are less than 0.35 and thus we are still able to assume that AERI's covariance matrix is diagonal. This noise filter was applied to all AERI observations used in this study.

While the AERI senses downwelling radiance in over 5000 spectral channels from 3.3 to 19 μm, not all of these channels are used in the retrieval. We are currently only using 324 spectral channels in our retrieval (see Table I) to avoid spectral regions where either there are overlapping gases contributing to the radiance or uncertainties associated with the spectroscopy.

TABLE I
AERI Spectral Regions Used in the Retrieval, and the Primary Sensitivity of Each Spectral Region

Starting Wavenumber [cm⁻¹]	Ending Wavenumber [cm⁻¹]	Primary sensitivity
538	588	Water vapor
612	618	Temperature
624	660	Temperature
674	722	Temperature
828	835	Clouds
843	848	Clouds
860	865	Clouds
872	877	Clouds
898	905	Clouds

B. Radiosonde

The current "gold standard" for thermodynamic profiling in the atmosphere is the radiosonde. Radiosondes have been used for many decades to provide temperature, humidity, and wind profiles throughout the troposphere for a wide range of applications. However, the temporal resolution of radiosonde launches is typically much less than 3-hourly, with the more traditional temporal resolution being 12-hourly, as radiosondes are expensive both in terms of consumables and man-power needed to launch them.

The ARM program has regularly launched radiosondes at its main facilities. The ARM program uses Vaisala radiosondes. For the validation portion of this study, model RS41 radiosondes were used at all three locations.

The AERIoe algorithm requires an *a priori* dataset to constrain the retrieval to realistic solutions, which is done by specifying the level-to-level covariance in the atmosphere. A large database of radiosondes is used for this purpose. The ARM program has historically launched RS92 sondes (from about 2004 until 2012) and RS80 sondes (prior to 2004). These long-term radiosonde records were used to build the climatologies needed to constrain the AERIoe algorithm. The dry bias that plagued the RS80 radiosonde (e.g., [31] and [32]) was not accounted for when these *a priori* datasets were constructed, as this bias had no impact on the covariance between any two levels.

A priori datasets were constructed for each ARM site for AERIoe. For the SGP site, radiosondes launched between 1992 and 2010 at a rate of 4 sondes/day were used. Due to the large number of radiosondes, a monthly prior was constructed and over 2000 radiosondes were used to build the prior for October. The Oliktok prior used data collected at the North Slope of Alaska (NSA) site [33], which is 220 km WNW of Oliktok, during the months of September, October, and November. At the NSA site, there are typically two launches per day, and over 1700 sondes were used to construct the prior for October. Finally, over 2700 radiosondes were launched as part of the 2-year GoAmazon project [34] at Manaus, which were typically 4/day, and these were used to build the prior for the Amazon retrievals.

C. Surface Meteorology

Surface meteorology observations (i.e., *in situ* measurements of temperature, relative humidity, and wind typically 2–10 m above the surface) are also a key component to most operational and research measurement strategies. The ARM program makes these observations at all of its facilities at 1-min resolution. Many passive radiometric retrieval methods benefit from the addition of these observations into the solution (e.g., [35]). This is a new observation that is added to the AERIoe retrieval framework. The uncertainties associated with these observations were assumed to be 0.5 °C for temperature and 3% for relative humidity (RH); however, the user has the ability to add a representativeness error to either of these if desired.

D. Numerical Weather Prediction Model

NWP models assimilate a wide range of data sources in order to get the initial state of the atmosphere correctly specified within the model before integrating the model forward in time to produce a weather forecast. These data sources could include hundreds-to-thousands of surface meteorology observations, synoptic radiosondes, satellite radiance, or geophysical product information, *in situ* observations made by aircraft, radar-observed wind, and precipitation fields, and more.

While many NWP modes are initialized every 3 h, the rapid-refresh (RAP) model [36] within the National Weather Service is initialized hourly, and thus hourly analysis fields are available. We will use the temperature and humidity fields from this model above the AERI location as additional "observation" into the AERIoe retrieval; however, we limit the observation only to heights above 4 km as NWP models have traditionally been less accurate in the boundary layer. To estimate the uncertainty of this "observation," we compute the standard deviation of the temperature and humidity fields at each height over a 100 km-by-100 km region to capture possible displacement error of the model of any synoptic boundaries.

E. Microwave Radiometer

Microwave radiometers (MWRs) are very similar to the AERI, in that they passively observe the radiation emitted by

the atmosphere albeit at microwave wavelengths. MWRs with multiple channels along the 22.2 GHz water vapor line and the 60 GHz oxygen absorption band are being used to profile the atmosphere also (e.g., [37] and [38]); however, their information content is about a factor of 2–3 times smaller than the information content in the AERI's observations [39], [40]. However, the combination of MWR with AERI observations has been shown to greatly improve the retrieval of liquid water path [10], and due to the differences in the vertical weighting function, may improve the retrieval of humidity also.

The ARM program primarily employs 2- and 3-channel MWRs at its sites [41]. The primary purpose of these instruments is to provide high temporal resolution profiles of PWV and liquid water path [41], [42]. All of these radiometers make measurements at 23.8 GHz (the side of the 22.2 GHz water vapor line) and at either 31.4 or 30.0 GHz (which is in an atmospheric window). These radiometers are calibrated via the automated collection of so-called "tip-curves" [41]. The noise level of these radiometric observations is approximately 0.3 K.

F. Raman Lidar

The ARM program has operated an automated Raman lidar for profiling water vapor, aerosols, and clouds since 1996 [43]. This lidar transmits 300 mJ pulses of laser energy at 355 nm vertically, and collects the backscatter at the laser wavelength and at two wavelengths associated with the Raman scattering by nitrogen (387 nm) and water vapor (408 nm) molecules with a 61-cm telescope [44]. The detection electronics combine both analog-to-digital and photon counting modes to provide backscatter profiles at 7.5-m, 10-s resolution [45]. These backscatter profiles are corrected for nonlinear system dead-time effects, the background is subtracted, and then the ratio of the water vapor to nitrogen signals is computed [46]. This ratio is proportional to the water vapor mixing ratio. Coincident radiosonde profiles are used to determine the near-field correction for mismatches between the fields-of-view of the two channels (the "overlap correction"), and the resulting profile is calibrated to match the mean of the radiosonde's water vapor mixing ratio between 2–3 km in clear skies. The Raman lidar is very stable, and thus the overlap correction and the calibration factor change very slowly with time.

To improve the signal-to-noise ratio of the data, the vertical and/or temporal resolution is typically degraded. While the Raman lidar is capable of profiling with 10 s and 75 m (e.g., [47]), we are using the ARM operational product which has resolutions of 10 min and 60 m in our analysis here.

III. APPROACH

A. Background

This infrared retrieval is an ill-posed problem. This means that there are multiple thermodynamic and cloud solutions that would agree with the radiance observations within the noise of the observations. To overcome this problem, the AERIoe algorithm uses an optimal estimation approach; an excellent overview of the optimal estimation technique is provided by the
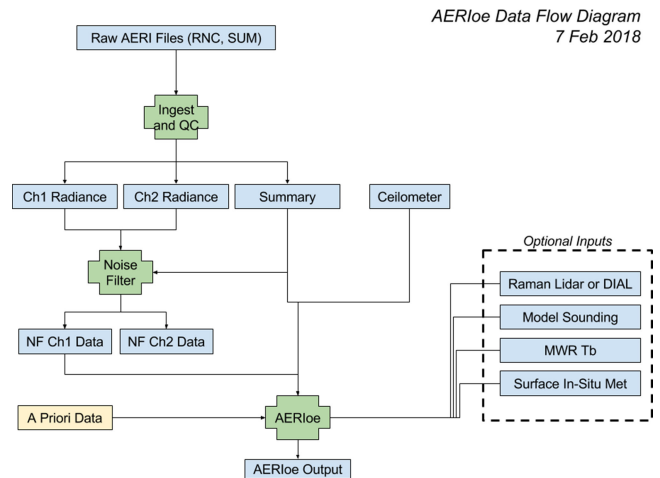

Fig. 3. Data flow diagram for the AERIoe algorithm. Version 2 is able to use the "optional input" datasets as additional inputs into the observation vector, thereby providing additional information for the retrieval.

work presented in [48]. Ultimately, the goal is to determine the optimal state vector $(\mathbf{X})$, which is the thermodynamic profiles and cloud properties, that satisfy both the observations $(\mathbf{Y})$ and the climatological information $(\mathbf{X_a})$, where the latter is used to constrain the solution.

B. AERIoe v1

The original version of the AERIoe algorithm (henceforth referred to as v1; [21]) utilized only the AERI observed radiance $(\mathbf{Y})$ and an *a priori* climatology $(\mathbf{X_a}, \mathbf{S_a})$ as input; cloud base height information from a collocated ceilometer was optional input (see Fig. 3). We desire to retrieve the state vector $\mathbf{X} = [\, T(z), q(z), L, R_{\text{eff, liq}}, \tau_{\text{ice}}, R_{\text{eff,ice}}, CO_2, CH_4, N_2O]^{T}$, where the superscript T denotes transpose, $T(z)$ and $q(z)$ are the desired temperature and humidity profiles as a function of height z, L is the liquid water path and τ_{ice} the ice cloud optical depth, $R_{\text{eff, liq}}$ and $R_{\text{eff,ice}}$ are the effective radii of the liquid and ice clouds, respectively, and CO_2, CH_4, and N_2O are parameters associated with the retrieval of the concentration of carbon dioxide, methane, and nitrous oxide, respectively. While cloud phase can be determined from the AERI if the atmosphere is semitransparent at 19 μm [8], [49], typically AERIoe is run with only liquid or ice clouds enabled (i.e., the prior is used to either fix L or τ_{ice} to zero). Furthermore, when v1 was under development, it was realized that the AERI had positive information content on the retrieval of these three trace gases; however, additional research was needed to demonstrate the accuracy that could be achieved (e.g., [50]); thus the retrieval of the three trace gas concentrations is usually disabled via the prior also. Therefore, in essence, the state vector used in AERIoe is usually $\mathbf{X} = [\, T(z), q(z), L, R_{\text{eff, liq}}]^{T}$.

To retrieve $\mathbf{X}$ from $\mathbf{Y}$, a forward model $\mathbf{F}$ is needed to convert $\mathbf{X}$ from the desired state space into the observational space $\mathbf{F}(\mathbf{X})$. In v1, the forward model used was the LBLRTM [51], [52]. This model has been heavily validated with AERI observations by the ARM program [12], [27]. The

last component needed is the Jacobian of F, which is defined as $\mathbf{K_{i,j}} = \partial \mathbf{F_i} / \partial \mathbf{X_j}$. $\mathbf{K}$ can be computed using finite differences, which involves running the LBLRTM for each perturbation of the elements of $\mathbf{X}$. Furthermore, due to the nonlinear nature of infrared radiative transfer, $\mathbf{K}$ depends on the current state vector, and thus should be updated for each iteration. This makes the retrieval computationally expensive, but techniques are used to approximate $\mathbf{K}$ thereby saving computation time without loss-of-accuracy. The computational speed of the retrievals needed to be fast enough for real-time processing during field experiments [53], which has the added benefit of making the retrieval capable of routine operation.

As AERIoe is an iterative retrieval, the first guess $\mathbf{X_1}$ is usually set equal to the prior mean $\mathbf{X_a}$. However, the use of the factor γ in (1), where γ changes in magnitude as the algorithm iterates, greatly stabilizes the retrieval and allows AERIoe to be insensitive to the first guess [54], [55]. Starting with the first guess, each subsequent iteration is computed as

$$X_{n+1} = X_a + \left(\gamma_n S_a^{-1} + K_n^T S_e^{-1} K_n\right)^{-1} K_n^T S_e^{-1}$$
$$\times \left(Y - F\left(X_n\right) + K_n\left(X_n - X_a\right)\right) \quad (1)$$

where the subscript n denotes the iteration number, and γ_n is the nth element of the vector $[1000, 300, 100, 30, 10, 3, 1, 1, 1, \ldots]$. The root-mean-square (RMS) difference between the observations and the forward model calculation is computed as

$$\text{RMS}_n = \text{sqrt}\left(\frac{1}{M}\sum_{i=1}^{M}\left(\frac{Y_i - F(X_n)_i}{\sigma_{Y_i}}\right)^2\right) \quad (2)$$

where M is the dimension of $\mathbf{Y}$. The retrieval continues to iterate until

$$\left(X_n - X_{n+1}\right)^T S^{-1}\left(X_n - X_{n+1}\right) \ll N \quad (3)$$

where N is the dimension of the state vector $\mathbf{X}$ [48], $\text{RMS}_{n+1} > \gamma_n \text{RMS}_n$, or the number of iterations exceeds some upper limit (usually 10). We will refer to the solution at the end of the iterations as $\mathbf{X_{opt}}$.

A nice feature of variational retrieval methods like AERIoe is that uncertainties in the observations and forward model are propagated to provide the uncertainties in the solution. This is done via the matrix $\mathbf{S_e}$. Ideally, $\mathbf{S_e}$ is specified as

$$S_e = S_Y + S_F = S_Y + K_{b,n} S_b K_{b,n}^T \quad (4)$$

where $\mathbf{S_Y}$ and $\mathbf{S_F}$ are the error covariance matrices of the observations and forward model, respectively. Frequently, $\mathbf{S_F}$ is assumed to be zero; however, in reality there are usually a large number of model parameters $\mathbf{b}$ that are uncertain. In the case of the LBLRTM, this includes the half-widths of absorption lines, the strength and temperature dependence of the water vapor continuum absorption, trace gas concentrations, etc. $\mathbf{S_b}$ represents the error covariance of these model parameters, and the Jacobian at $\mathbf{b}$ at $\mathbf{X_n}$ should be computed as $(\mathbf{K_{b,n}})_{i,j} = \partial \mathbf{F}(\mathbf{X_n})_i / \partial \mathbf{b_j}$ to translate $\mathbf{S_b}$ into the observational space spanned by $\mathbf{S_e}$. However, like $\mathbf{K_n}$, $\mathbf{K_{b,n}}$ is also dependent upon the current state vector $\mathbf{X_n}$; thus properly accounting for the uncertainty in $\mathbf{b}$ would greatly increase the computational cost of the retrieval. To overcome this, we assume $\mathbf{S_F}$ is zero and inflate the uncertainty associated with the

observed radiances (i.e., we inflate $\mathbf{S_Y}$); we actually use the AERI radiance uncertainty before the PC noise filter is applied, and thus the 1-σ values used to build $\mathbf{S_Y}$ are about four times larger than their true values (as the radiance data used in $\mathbf{Y}$ are the noise filtered data). We have found this to be a good compromise between capturing the uncertainties in the forward model and computational speed.

The uncertainty of the retrieved product is a direct output of this optimal estimation method, and is characterized by the posterior covariance matrix. This matrix $\mathbf{S_{opt}}$ is computed as [21], [54], and [55]

$$S_{\text{opt}} = B^{-1}\left(\gamma_n^2 S_a^{-1} + K_n^T S_e^{-1} K_n\right) B^{-1} \quad (5)$$

where

$$B = \gamma_n S_a^{-1} + K_n^T S_e^{-1} K_n. \quad (6)$$

This covariance matrix $\mathbf{S_{opt}}$ provides the full error characterization of the retrieval, and can be sampled using Monte Carlo techniques to see the range of valid solutions (e.g., [21]). However, more typically, the square root of the diagonal of this matrix is used to specify the 1-σ errors in the profiles of temperature and humidity.

C. AERIoe v2

The v1 was used to process many AERI datasets, including data collected by the fixed and mobile profiling stations during the plains elevation convection at night field campaign [56]. Analysis of these data demonstrated several nonphysical attributes, such as the potential temperature decreasing markedly with height and levels where the relative humidity was greater than 100%. Constraints were added to the new version of AERIoe to prevent both of these events. In the case of the latter, the water vapor mixing ratio was decreased such that the RH was limited to 100% or less for each iteration; these changes were always within the uncertainty of the water vapor retrievals. For the former, we recognized that superadiabatic layers can exist, especially near the surface. Thus, we force the potential temperature profile to monotonically increase with height above the specified height of any superadiabatic layer, which is specified in the AERIoe configuration file by the user. In both the RH and potential temperature adjustments, an additional iteration is required by the algorithm after the adjustment. Generally, these two adjustments work to help differentiate between two different thermodynamic solutions to the observed radiance (i.e., to overcome the ill-posed nature of the solution).

Second, there was a desire to improve the accuracy of the AERIoe retrievals relative to comparisons radiosondes and other sensors. While we are only using a portion of the infrared spectrum for our retrievals due to inconsistencies in the accuracy of the infrared spectroscopy [21], we felt it was more efficient to incorporate additional observational data streams into the AERIoe retrieval. This was also done in the AERIprof development [18], [19] and produced a noticeable improvement in their retrievals. However, a key difference is that these additional observations were used to construct a better first guess for the AERIprof, whereas in AERIoe these additional observations are included in the observation vector $\mathbf{Y}$ so that the retrieval algorithm has to

find a solution that agrees within their uncertainties also. A key aspect of these new datasets for inclusion in the AERIoe is that they be operational (i.e., always available) and consistent with the AERI observations.

As indicated above, the AERIoe v1 only used AERI data in the observational vector $\mathbf{Y}$. However, given this formulation before, there is no restriction on the observations that are incorporated into $\mathbf{Y}$, as long as there is a forward model that can be used to translate between the state vector space into the observational space. Thus, the observation vector can be written as $\mathbf{Y} = [\mathbf{Y_{AERI}}, \mathbf{Y_{other}}]^T$, the observational covariance matrix as

$$S_Y = \begin{bmatrix} S_{\mathrm{AERI}} & 0 \\ 0 & S_{\mathrm{other}} \end{bmatrix} \qquad (7)$$

as we will assume there is no covariance between different instruments, and the forward model is $\mathbf{F} = [\mathbf{F_{AERI}}, \mathbf{F_{other}}]^T$, where $\mathbf{F_{AERI}}$ is the LBLRTM and $\mathbf{F_{other}}$ is the appropriate forward model. The Jacobian is computed the same way, namely as

$$K_n = \begin{bmatrix} \frac{\partial F_{\mathrm{AERI}}}{\partial X_n} & \frac{\partial F_{\mathrm{other}}}{\partial X_n} \end{bmatrix} \qquad (8)$$

where $\mathbf{K_n}$ has dimensions M = (number of AERI channels plus number of "other" observations) by N.

It is important to note that the units of the observations from the different instruments do not have to be the same. Indeed, (1) shows that the difference between the observations and the forward model is normalized by the observation covariance matrix $\mathbf{S_e}$, which makes the problem unitless at that point. This approach has already been demonstrated in a simplistic way, wherein AERI and MWR observations were combined in the observation vector to provide an improved retrieval of liquid water path [10].

Thus, for some observation types such as surface meteorology or NWP output, the forward model is trivial; it is just an interpolation from the retrieval's vertical grid to the height of the surface *in situ* sensor or NWP model level, and the Jacobian for that model is just as trivial. While the state vector in AERIoe uses ambient temperature and water vapor mixing ratio, it is trivial to translate these into relative humidity for use with the surface meteorology observations. The Raman lidar's water vapor profiles are also easily incorporated into AERIoe via the same logic. To give the user flexibility with these, the retrieval's configuration file can be modified to inflate the error in the Raman lidar or NWP profile observations, specify the height range over which they should be used, or add representativeness errors to any of them.

Incorporating the MWR observations into AERIoe requires the use of a microwave radiative transfer model. We use the MonoRTM [52], which has the same physical basis as the LBLRTM. This model has also been heavily validated against ARM and other observations, with many components including the water vapor continuum [57], [58], the oxygen absorption parameters [59], [60], and the liquid water absorption model [61] being updated. The AERIoe can use any number of microwave frequencies in the retrieval; the configuration file used
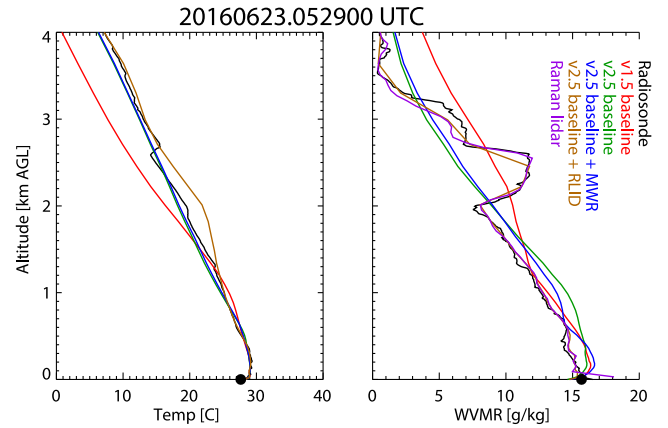

Fig. 4. Temperature (left) and water vapor mixing ratio (right) profiles observed by the radiosonde (black) and retrieved using various versions/configurations of the AERIoe retrieval algorithm (red, green, blue, brown). The Raman lidar's water vapor observation is also shown (purple). This is a night-time profile at 0529 UTC on 23 June 2016 at the SGP site. The surface-based *in situ* meteorological observations are the black dots.

to control the algorithm that specifies the center frequencies of the channels, the noise levels, etc.

The primary challenge with incorporating different observations together in the retrieval is that the observations, and the associated forward models, must all be consistent. We have elected to not use the 89 GHz channels in the ARM 3-channel MWRs in our retrieval, for example, because it has proven difficult to keep that particular channel well calibrated. The optimal estimation framework assumes that the observations and forward models are unbiased, and thus a bias in an observation will work to bias the retrieval, where the magnitude of the bias depends on the sensitivity of the forward model and the random uncertainty in the observation itself.

For routine use of AERIoe, we use RAP output from 4 km above the ground to the tropopause and surface meteorological observations together with AERI radiances; we consider this the baseline for v2 as both of these additional observations are available at virtually all sites where there are AERIs. The Raman lidar is a research lidar and only available at a few sites; thus, using data from this system is indicative of what may be possible if a water vapor lidar (of any type, including differential absorption systems like [62]) is collocated with the AERI.

IV. RESULTS

A. Case Study

Examples of the AERIoe retrieval using v1 and v2 with different input datasets are shown in Fig. 4 (night-time) and Fig. 5 (daytime); these profiles, which were collected 12 h apart at the SGP site, represent the typical performance of each retrieval configuration. The temperature retrievals agree very well with the radiosonde below 1 km, although the lack of the superadiabatic constraint in the v1 profile daytime retrieval (see Fig. 5, red curve) is obvious. Further, the addition of the RAP data above 4 km greatly improves the v2 temperature retrieval from 3 km and above; there is less than 10% of the total AERI information content associated with heights above 3 km [21, Fig. 7c].
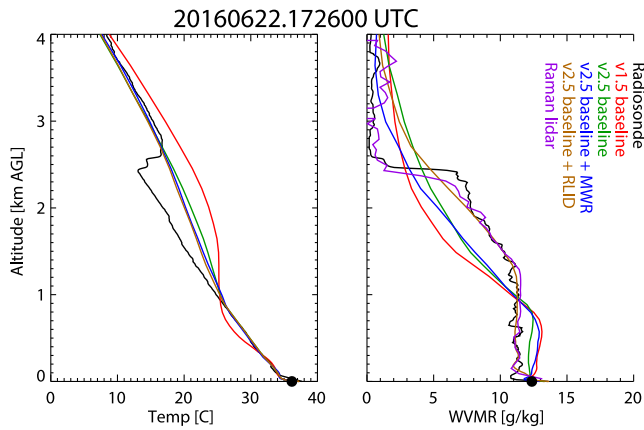
Fig. 5. Same as Fig. 4, except a daytime profile at 1726 UTC on 22 June 2016 at the SGP site.
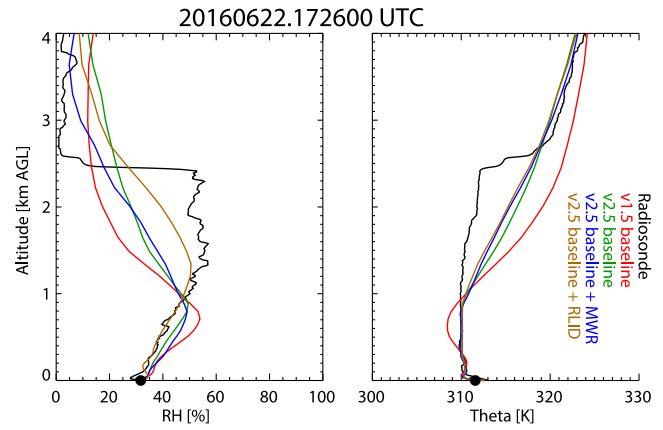

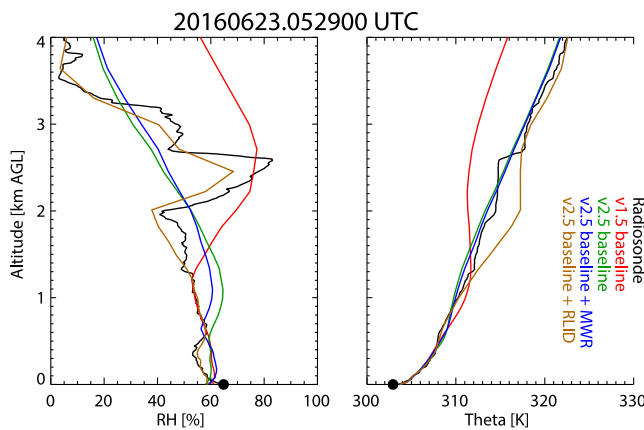Fig. 7. Same as Fig. 6, except a daytime profile at 1726 UTC on 22 June 2016 at the SGP site.

Fig. 6. RH (left) and potential temperature (right) profiles derived from observations made by the radiosonde (black) and retrieved using various versions/configurations of the AERIoe retrieval algorithm (red, green, blue, brown). This is a night-time profile at 0529 UTC on 23 June 2016 at the SGP site. The surface-based *in situ* meteorological observations are the black dots.

However, none of the AERIoe retrievals are able to capture the sharp inversion at the top of the convective boundary layer at 2.5 km (see Fig. 5), or the more subtle inversion at the top of the residual layer at night at the same level (see Fig. 4). Interestingly, the retrieved profiles were already in good agreement with the surface observations (see Figs. 4–7, black dots at the surface), and thus there was little obvious impact by adding these observations. Indeed, the addition of the surface temperature *in situ* observation adds almost no information to the retrieval, as the degrees of freedom for signal (DFS) changes by less than 0.1, whereas the addition of the surface RH observation increases the DFS in the humidity profile by 0.2 to 0.5, depending on the situation.

The RAP data also improved the v2 water vapor retrieval, especially for heights above 3 km where less than 15% of the AERI's information content is above that height [21, Fig. 7e]. The addition of the MWR observations has a relatively small impact on the retrieved humidity profile. The AERIoe data hint at a well-mixed boundary layer during the daytime (see Fig. 5) below 1 km, but the vertical resolution of the retrieval

[21, Fig. 7f], which gets poorer with altitude, results in a smoothing of any moisture gradients and thus a wet bias below 1 km and moist bias between 1 and 2.5 km.

The addition of the Raman lidar moisture profile, which was used in the v2 retrieval starting at 100 m above the surface, showed excellent agreement with the radiosonde profile at night (see Fig. 5) over this entire height range (0 to 4 km) including the moisture inversion between 2.0 and 2.5 km. We should note that including active water vapor lidar data into a passive MWR thermodynamic retrieval was done by the work presented in [63], but this is the first time it has been used in a spectral infrared retrieval. The AERIoe retrieval that used the Raman lidar data agrees almost perfectly with the Raman lidar observations, which demonstrates that the information content on water vapor in the lidar is markedly larger than in the AERI, which agrees with the results from the work presented in [63]. During the daytime, this excellent agreement was limited to heights below 2.5 km; the random error in the Raman lidar (which is largest during the daytime) prevents the retrieval from capturing that rapid decrease. Interestingly, while the night-time retrieval that used the Raman lidar data captured the moisture inversion well, it also resulted in a warm temperature bias at about the same altitude. We will show later that typically the inclusion of the Raman lidar water vapor data had little-to-no impact on the retrieved temperature profile.

Often, new insights can be found when the retrievals are studied in different ways. Figs. 6 and 7 show the derived RH and potential temperature (theta) profiles for the same cases. In both the night-time (see Fig. 6) and daytime (see Fig. 7), the v2 retrievals agree much better with the radiosonde observations than the v1 retrievals. The potential temperature retrievals clearly demonstrate the improvement afforded by the constraint that theta should not decrease with altitude, as both the v1 and v2 profiles yield solutions that agree with the AERI radiance observations within their uncertainty. The inclusion of the RAP data improves both RH and theta profiles.

The impact of including the different observations into the retrieval are perhaps most easily seen by investigating the 1-σ uncertainty profiles that were derived from $\mathbf{S_{opt}}$. These are shown for our two cases in Figs. 8 and 9. For both temperature
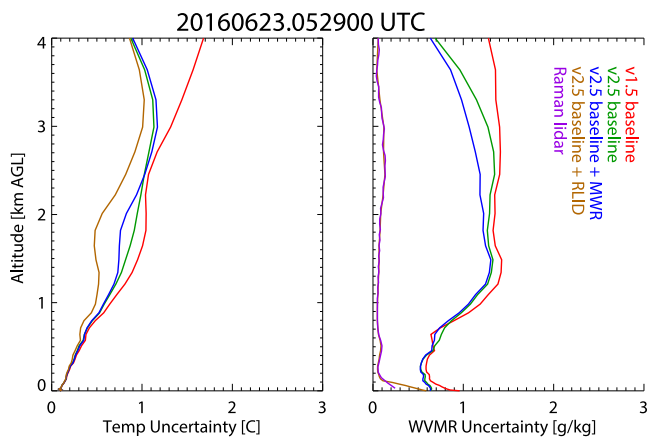
Fig. 8. 1-σ uncertainties in the AERIoe retrievals for different versions/configurations (red, green, blue, and brown) for temperature (left) and water vapor mixing ratio (right). The uncertainty in the Raman lidar water vapor observation is also shown (purple). This is the night-time case on 0529 UTC on 23 June 2016 at the SGP site.
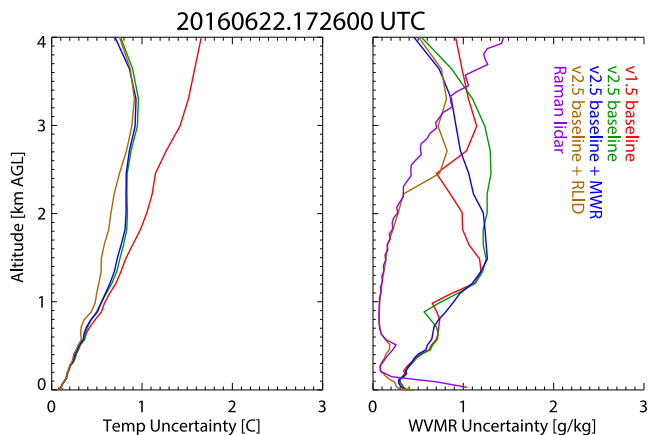

Fig. 9. Same as Fig. 8, except a daytime profile at 1726 UTC on 22 June 2016 at the SGP site.

and humidity, including more observations in the retrieval reduces the uncertainty in the retrieval. The RAP data have the largest impact above 3 km, which is expected given that the AERI's information content at those heights is small. The addition of the MWR data has little-to-no impact on the uncertainty in the retrieved temperature profile, and its impact on the water vapor profile is concentrated between 2 and 4 km. The Raman lidar observations have markedly different impacts day versus night due to the strong dependence of the random noise levels in the lidar to ambient light. Generally, though, including the Raman lidar observations greatly decreases the uncertainty in the water vapor retrievals at all levels and has a small but positive effect on the temperature retrievals above 1 km. The extremely low uncertainty level in the temperature retrievals near the surface, which is due to the AERI's high information content at those levels, results in very accurate measurements of the lapse rate in the lowest 100 m [64].

Note that we did not anticipate that there would be any impact on the retrieved temperature profile when the MWR brightness temperature data were included in the retrieval. The ARM

program's MWRs primarily are two- or three-channel systems that were selected to provide information on the PWV and liquid water path above them [41]; these channels have virtually no sensitivity to changes in the atmospheric temperature. Similarly, we did not anticipate that the addition of the Raman lidar water vapor observations in the retrieval would have a significant impact either. In both cases, the minor improvement in the retrieved temperature is almost certainly due to the improved water vapor retrieval and its influence on the temperature via the covariance between the temperature and water vapor in the prior.

The 1-σ uncertainty profiles are illuminating, but the impacts of adding the additional observations on the posterior covariance matrices is stark. Passive spectral radiometers, such as the AERI, possess far less information in their observations than the number of vertical levels in the retrieved profiles. The AERI radiance observations has between 5–8 and 3–8 independent pieces of information on the temperature and water vapor profiles, respectively [21], [40]; these numbers are much smaller than the 55-level vertical grid currently used in the AERIoe retrievals. As a consequence, the retrieval will use observations together with the vertical weighting functions that result from the forward model, constrained by the level-to-level correlation in the prior $\mathbf{S_a}$, to get the solution. The resulting level-to-level correlation is captured in the posterior covariance matrix $\mathbf{S_{opt}}$. The ideal $\mathbf{S_{opt}}$ matrix would be one where all off-diagonal elements are zero; this would imply no level-to-level covariance and thus the retrieval would have perfect information on each level.

The $\mathbf{S_a}$ used in the SGP retrievals shown in Figs 3–9, as well as the resulting $\mathbf{S_{opt}}$, were converted to a correlation matrix and visualized in Fig. 10. The temperature data in the prior [see Fig. 10(a1)] are highly correlated (r > 0.5) between any two levels for heights less than 5 km. This correlation is primarily due to the fact that temperature decreases at a regular rate with height in the troposphere (i.e., due to the lapse rate). The water vapor prior [see Fig. 10(a3)] also shows relatively high correlations, especially between any two levels that are less than 1km apart.

The $\mathbf{S_{opt}}$ that results from v1 [see Fig. 10(b1) and (b3)] shows a much lower level-to-level correlation in general, although the reduction of the information content in the AERI observations with height results in correlations greater than 0.4 for any two heights above 2.5 km for the retrieved temperature [see Fig. 10(b1)]. The v1 water vapor retrieval also greatly reduces the level-to-level covariance, although an interesting band of negative correlation (the blue semicircular like band) is added [see Fig. 10(b3)]. The 1-σ uncertainty profiles, which is the square root of the diagonal of the covariance matrices for the prior (dot-dashed) and the retrieval (solid) in Fig. 10(b2) and (b4), show that the retrieved profile has a much smaller uncertainty than the prior.

The addition of the other datasets into the retrieval further improves the posterior covariance matrices relative to the v1 posterior solution. In particular, the RAP data greatly reduce the level-to-level correlations above 2 km in both the temperature and water vapor (see Fig. 10, rows b, c, d, and e), and removes the semicircular negative correlation band that was seen in the v1
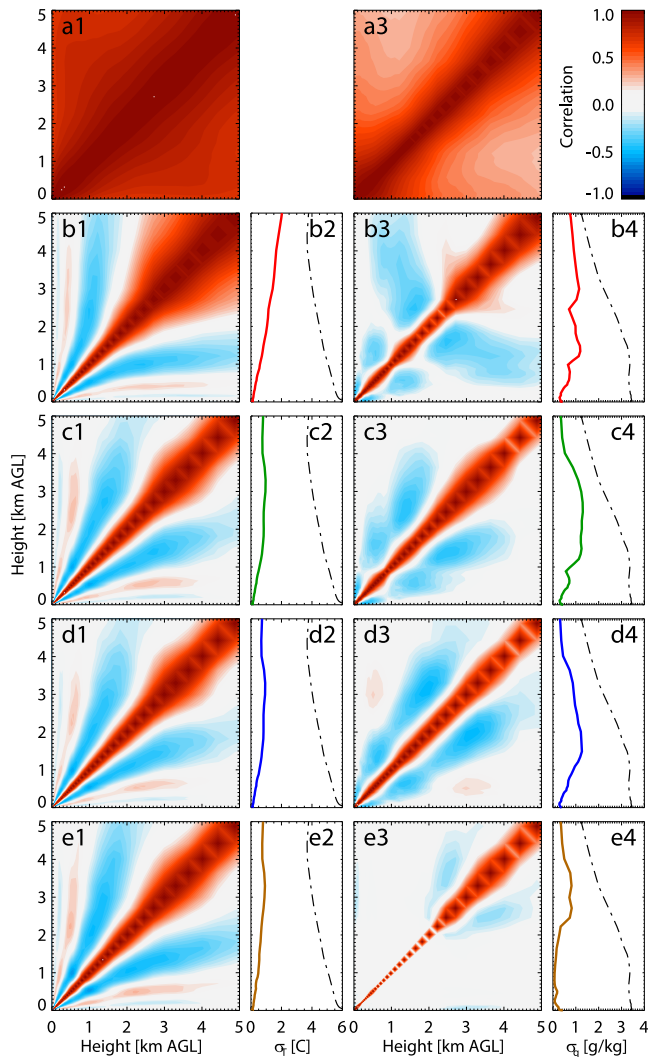
Fig. 10. Prior correlation matrix for temperature (a1) and water vapor (a3) retrievals within AERIoe. The posterior correlation matrix for temperature [panels (b1), (c1), (d1), and (e1)] and water vapor [panels (b3), (c3), (d3), and (e3)] for the AERIoe v1 baseline (row b), v2 baseline (row c), v2 baseline with MWR data (row d), and v2 baseline with Raman lidar data (row e). Columns 2 and 4 show the 1-σ uncertainties in temperature and water vapor, respectively, for each retrieval method as solid lines, where the 1-σ uncertainties in the prior are shown as dot-dashed lines. This is a daytime case at 1726 UTC on 22 June 2016 at the SGP site.

results [compare Fig. 10(c3) to (b3)]. The inclusion of the MWR or Raman lidar data have virtually no impact on the character of the temperature posterior covariance [compare Fig. 10(d1) and (e1) to (c1)]. Adding the MWR data to the retrieval reduces the correlation between nearby levels especially above 3 km [i.e., the red band going up the diagonal of Fig. 10(d3) is narrower than that in Fig. 10(c3)], but there is a slight increase to the height of the negative correlation structure. The addition of the Raman lidar data greatly improves the water vapor posterior covariance matrix [see Fig. 10(e3)], with large portions of that matrix very close to zero, even for layers that are adjacent to each other. This is a daytime example, and thus the increase of the random error in the lidar's data with height results in the appearance of some nearby level-to-level correlation for heights above 2.5 km. During the night-time, when the Raman lidar's

noise profile is tiny throughout the entire profile (see Fig. 8, purple curve), the water vapor posterior correlation matrix is effectively a unit matrix

B. Statistics for Different Input Datasets

The case study examples allow details of the retrieved profiles to be illuminated, but how representative are these examples? In particular, did the addition of either the MWR or Raman lidar observations markedly improve the retrieved profiles relative to the v2 baseline that used the RAP output and surface meteorology observations? To evaluate this, comparisons were made between AERIoe retrievals and radiosonde for the entire month of October 2016 using data from SGP site. Cases with clouds below 2 km were omitted, as clouds quickly become opaque in the infrared as the liquid water path increases. There were several examples where the MWR data were unavailable, leaving 94 comparisons between the measurement techniques.

Traditional methods used to evaluate retrieved profiles against radiosondes compute the mean and standard deviation of the differences with height. These bias (solid lines) and standard deviation profiles (dot-dashed lines) are shown in Figs. 11(a) and 12(a) for temperature and water vapor, respectively. For temperature, the standard deviation profiles are virtually identical, increasing nearly linearly from 0.4 °C at the surface to 1.5 °C at 3 km. Including the MWR data changes the bias profile relative to the other two cases, with a slight reduction of bias between 1.0 and 1.5 km and a slight increase in the absolute bias above 2.2 km. However, in all three datasets the mean absolute bias is less than 0.5 °C. This level of accuracy is what was suggested by the case study examples.

The water vapor bias and standard deviation results also support the conclusions from the case study examples as well. Including the MWR observations eliminates the bias above 1.8 km and reduces the standard deviation above that level by approximately 20%. Including the Raman lidar data results in a bias near zero above 300 m and a standard deviation profile less than 0.3 g/kg. The bias below 300 m can be attributed to a systematic error in the overlap correction; Bayesian retrievals like AERIoe are largely unable to remove systematic errors like this.

While the bias and standard deviation profiles are informative, these statistics can hide many details. They show that the retrieved profiles have little bias, but does a particular configuration of the retrieval (i.e., using one particular set of additional instruments) capture the shape of the retrieved profiles better than a different retrieval configuration? To investigate this, we use the so-called modified Taylor plots [21], wherein each retrieval/sonde pair is used to derive the correlation coefficient (cc) from the surface to 3 km and the ratio of the standard deviations ($rs = \sigma_a / \sigma_s$), where σ_x is the standard deviation of the profile over that same height range from the AERIoe retrieval ($x = a$) and radiosonde ($x = s$). These ordered pairs (cc, rs) are plotted for the v2 baseline [panels (b)], v2 baseline with MWR [panels (c)], and v2 baseline with Raman lidar [panels (d)] for both temperature (see Fig. 11) and water vapor (see Fig. 12).

The modified Taylor plots for temperature show virtually no difference between the v2 baseline [see Fig. 11(b)] and the retrievals that include MWR data [see Fig. 11(c)]. The black
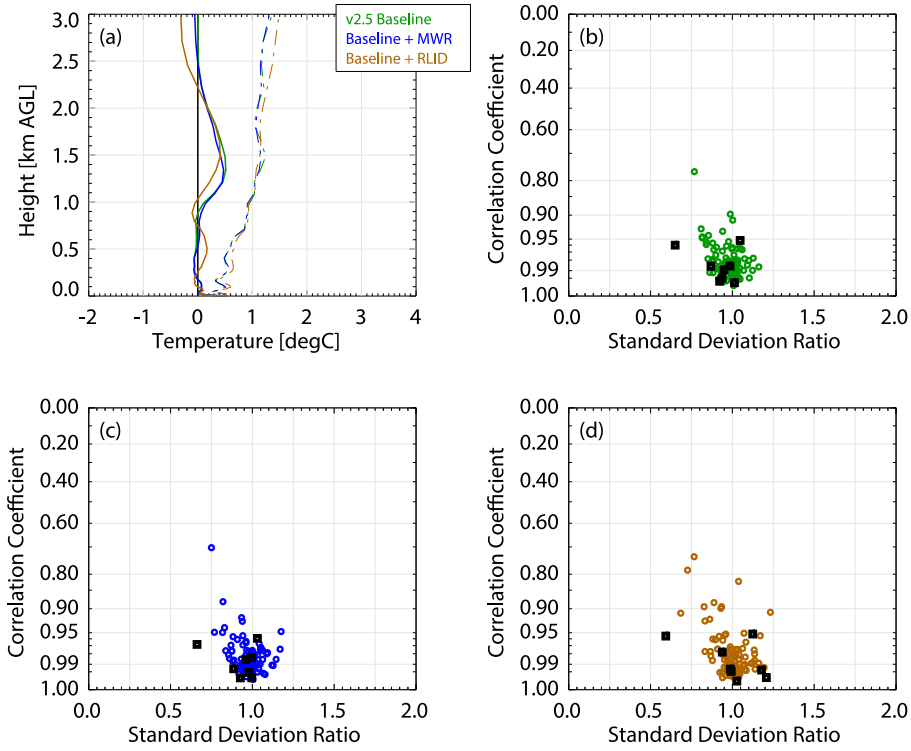
Fig. 11. Panel (a) shows the bias (solid) and RMS (dot-dashed) profiles for temperature from the v2 baseline retrieval (green), the baseline with MWR observations (blue), and the baseline with Raman lidar observations (brown). Panels (b), (c), and (d) show modified Taylor plots comparing these three AERIoe configurations (respectively) to radiosonde temperature data from the surface to 3 km. There are 94 cases from the SGP site from October 2016. The black squares in panels (b), (c), and (d) denote cases where the observation is more than 1 standard deviation away from the climatological mean.
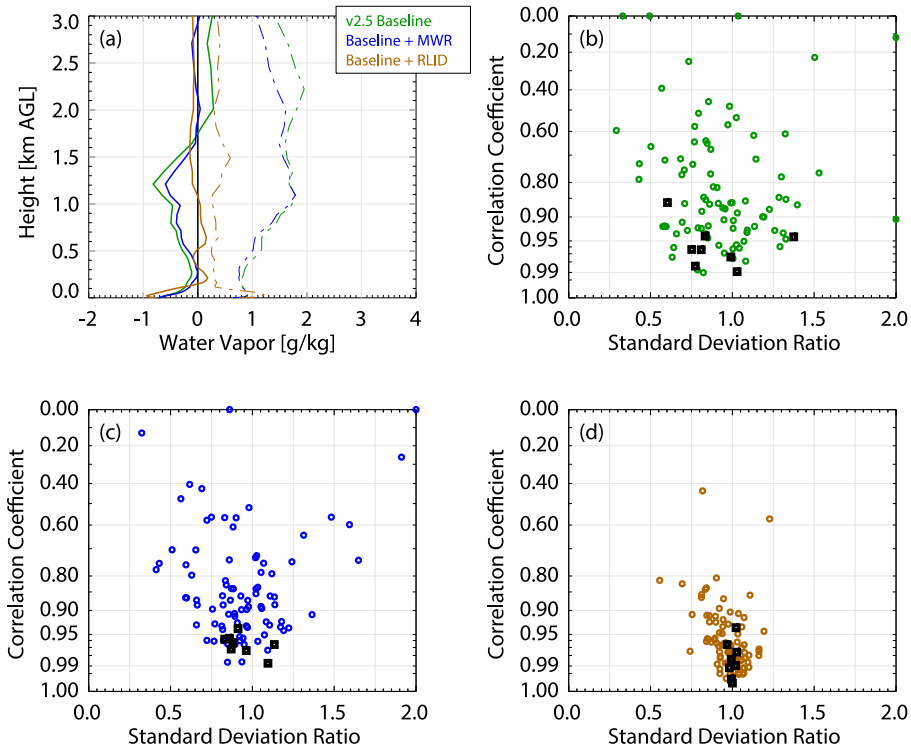

Fig. 12. Same as Fig. 11 except for water vapor.

TABLE II
THE 25TH, 50TH, AND 75TH PERCENTILES OF THE STANDARD DEVIATION RATIO AND CORRELATION OF THE PROFILES FROM THE SURFACE TO 3 KM FOR BOTH TEMPERATURE AND WATER VAPOR FOR THE DATA SHOWN IN FIGS. 8 AND 9. THE MEDIAN VALUES ARE BOLDED. THERE ARE 94 PROFILES IN THIS COMPARISON

	Temperature StDev Ratio	Temperature Correlation	Water Vapor StDev Ratio	Water Vapor Correlation
v2 Baseline	0.93, **0.99**, 1.02	0.97, **0.99**, 0.99	0.76, **0.91**, 1.08	0.72, **0.88**, 0.94
Baseline + MWR	0.93, **0.98**, 1.01	0.98, **0.99**, 0.99	0.82, **0.91**, 1.06	0.76, **0.89**, 0.94
Baseline + RLID	0.94, **1.00**, 1.04	0.97, **0.99**, 0.99	0.92, **0.99**, 1.04	0.94, **0.97**, 0.99

squares denote points that are further than 1 standard deviation away from the mean of the *a priori* dataset as measured with a χ^2 coefficient; these are presumably more challenging for the retrieval algorithm to get correct than samples that are close to the mean of the *a priori* [38]. There is virtually no difference in the distribution of the black squares in Fig. 11(b) and (c) either. However, the inclusion of the Raman lidar observations increases the spread in both the *rs* and *cc* coefficients, albeit only slightly. This suggests that the slight impact we saw on the temperature profile above 2 km in Fig. 4 may occur occasionally when Raman lidar data are used in the retrieval, and that the case study example was not an anomaly.

The modified Taylor plots for water vapor (see Fig. 12) show a different story. Including the MWR data [see Fig. 12(c)] reduces the spread in both the *cc* and *rs* coefficients relative to the baseline results [see Fig. 12(b)], especially for the points that are far from the mean prior (black squares). Including the Raman lidar observations [see Fig. 12(d)] greatly reduces the spread in the *cc* and *rs* coefficients, and moves their median values much closer to the ideal (1, 1) point (see Table II). These results clearly show the value of adding the Raman lidar observations, as the water vapor (*cc, rs*) statistics are now nearly identical to temperature (*cc, rs*) statistics in the v2 baseline results (see Table II).

C. Accuracy in Cloudy Conditions

The AERIoe algorithm is able to retrieve thermodynamic profiles in both clear and cloudy conditions. A natural question is to ask: what is the accuracy of the retrieved profiles in cloudy relative to clear sky conditions?

The bias and RMS statistics of clear sky versus cloudy sky profiles for Oklahoma and German sites were presented in [6] and [40], respectively; these papers demonstrated that the bias and RMS profiles were very similar between clear sky and cloudy cases. However, in those analyses, all of the cloudy data were grouped in a single bin and the impact of the cloud on the accuracy of the retrieved thermodynamic profile around the cloud boundary was not determined. Due to the broadening of the radiative weighting functions with height, it may be difficult to accurately retrieve temperature and humidity close to the cloud base. Because cloud base spans a wide range of heights, it is difficult to get good statistics that assess AERIoe performance in environments with clouds at different levels (e.g., with cloud bases between 800 and 1000 m) without processing thousands of cases.

However, a high temporal resolution retrieval in a case with broken clouds can illustrate the relative accuracy of the clear versus cloudy sky retrievals. Fig. 13 provides an example during a fair weather cumulus case using the v2 algorithm. The black dots indicate the cloud base height for clouds where the retrieved liquid water path is above 10 g m^{-2} (which is approximately an optical depth of 1 for these clouds). Just below the clouds, the temperature profile is several degrees cooler relative to the retrieved temperature at the same height between the clouds. This bias, which isn't seen in all examples and isn't readily apparent in the retrieved water vapor profiles, demonstrates the challenges of separating the cloud emission from the emission by the atmosphere just below the clouds when the weighting functions become broad.

However, using the vertical resolution, which can be derived from the averaging kernel [48], [21], we can estimate the range of retrieved data points below the cloud that is potentially affected by the cloud. This is indicated by the small blue/brown symbols plotted under the clouds in Fig. 13. Below these symbols, there is very good temporal consistency. Therefore, analysis of the retrievals in cloudy conditions should focus on data that are below the cloud base height minus the one half of the vertical resolution at cloud base. This vertical resolution profile is a standard output product from AERIoe [21], [40].

D. Impact in the Arctic and Tropics

The information content in the AERI observations is a function of the PWV, as increasing PWV will result in some absorption lines becoming opaque and thus there is less information content overall in the spectra [21]. The range of PWV at the SGP site in October 2016 was relatively wide, ranging from 0.5 cm to more than 4 cm. However, to illustrate the capabilities in other climatic regimes, we have included additional profiles from Oliktok, Alaska, during October 2016 where the PWV ranges from about 0.1 to 1 cm and from the AMF data collected in the Amazon in June 2015 when the PWV ranged from 4 to over 6 cm (see Fig. 1). As there aren't Raman lidars at these two sites, and there was some concern about the calibration of the MWR at Oliktok, we compared the v1 results against the v2 baseline (which use NWP output and surface meteorology observations) results.

The bias (solid) and standard deviation (dot-dashed) profiles for the v1 results for the three locations are shown in Fig. 14. The bias profiles show significant temperature errors [see Fig. 14(a)] between 300 and 1.2 km for the SGP and Oliktok data, and a
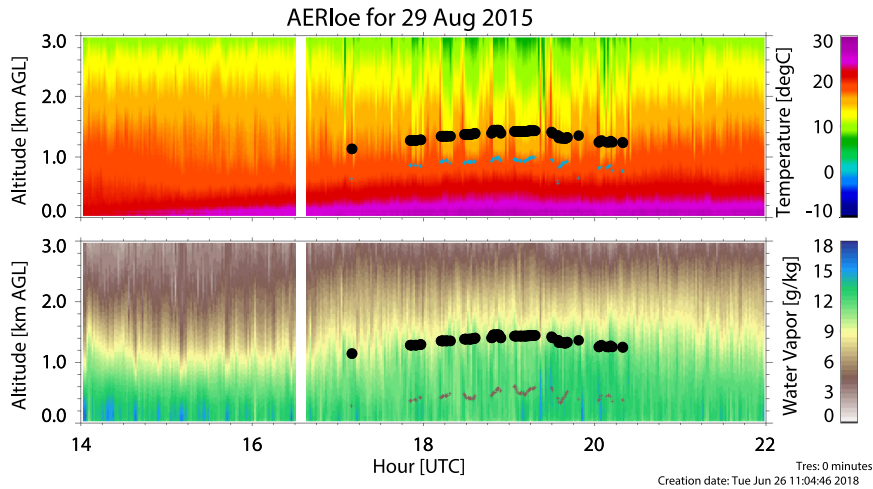
Fig. 13.   High-resolution (~30 s) retrieval of temperature (top) and humidity (bottom) at the SGP site on 29 August 2015. Black dots indicate the height of cumulus clouds with liquid water paths above 10 g m^{-2}. The small blue/brown dots indicate the maximum height that is not influenced by the emission by the cloud, as determined from the vertical resolution at the cloud base. See text for more details.
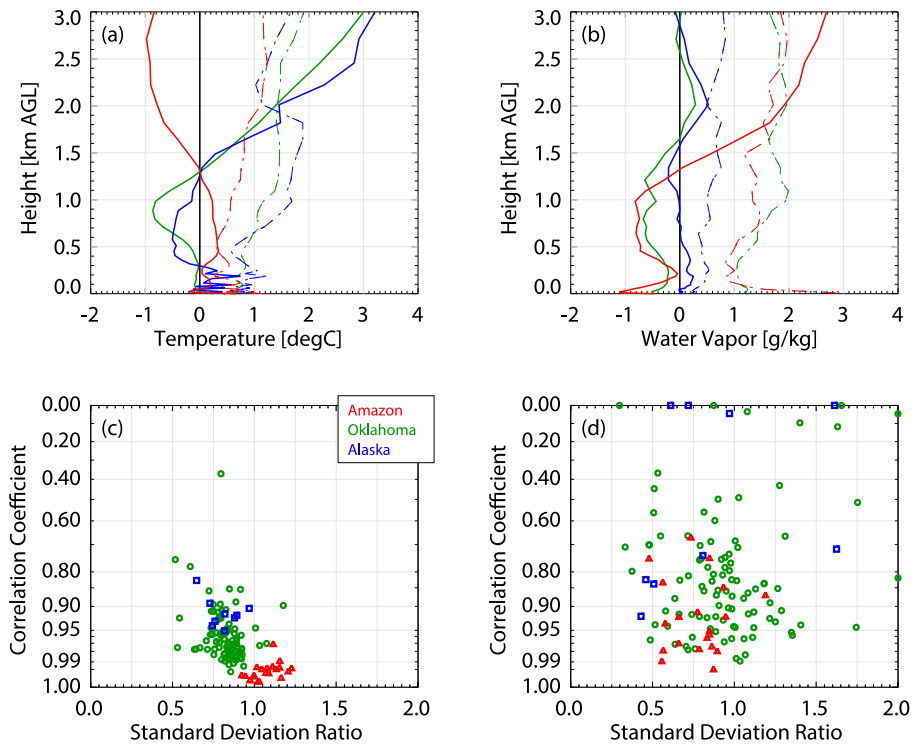

Fig. 14.   Bias (solid) and RMS (dot-dashed) profiles between radiosondes and the AERIoe v1 retrieval for temperature (a) and water vapor (b) using the 139 cases from Alaska (blue), Oklahoma (green), and the Amazon (red). Panels (c) and (d) show the associated modified Taylor plots for temperature and water vapor, respectively.

large growing bias above 1.5 km for the Amazon data. The water vapor bias at Oliktok is very small for the entire 3 km range, but there is an order 0.5 g/kg bias in both the SGP and Amazon water vapor profiles below 1.2 km [see Fig. 14(b)], with the bias in the Amazon retrievals changing sign and growing substantially above 1.5 km. The difficulties in retrieving water vapor for the Amazon site, especially above 1.5 km, is likely due the much smaller information content there due to the high PWV values.

The modified Taylor plots for temperature [see Fig. 14(c)] and water vapor [see Fig. 14(d)] show significant scatter in both *cc* and *rs*.

However, the additional physical RH and theta constraints in v2 together with the NWP and surface observations greatly improve the retrieved profiles (see Fig. 15). The temperature biases are all much smaller relative to the v1 results, especially for the SGP and Oliktok sites. At Oliktok, the v2 bias is very close to
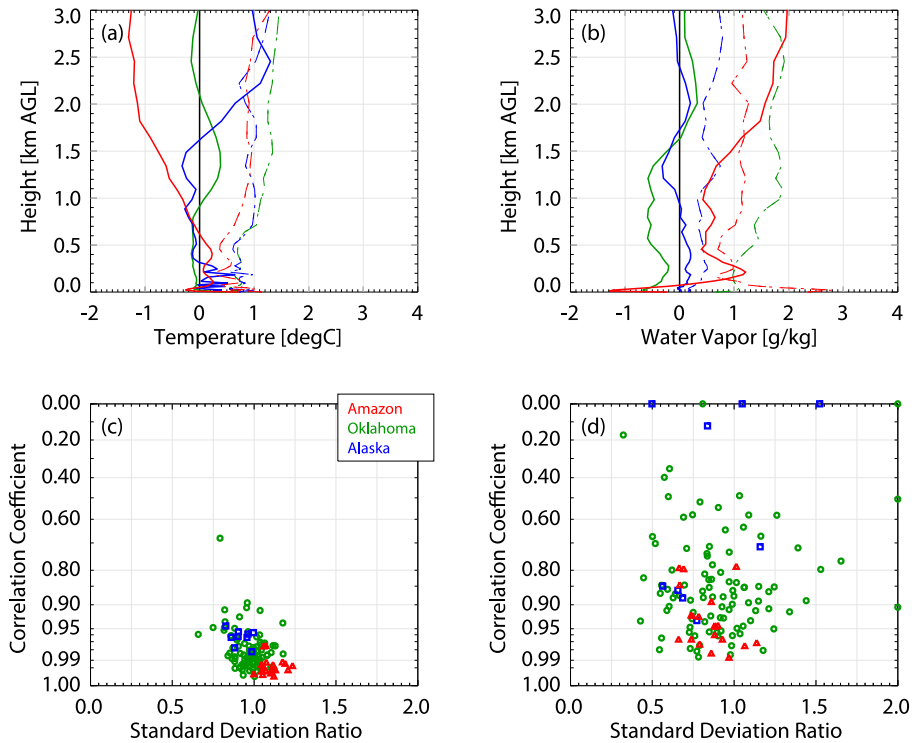
Fig. 15. Same as Fig. 14 except for AERIoe v2 baseline retrievals.

TABLE III
Same as Table II for the Data Shown in Figs. 11 and 12. There are 139 Profiles in This Comparison, of which 12 are From Oliktok (Alaska), 107 are From the SGP (Oklahoma), and 20 are From the Amazon

	Temperature StDev Ratio	Temperature Correlation	Water Vapor StDev Ratio	Water Vapor Correlation
v1	0.80, **0.86**, 0.97	0.95, **0.98**, 0.99	0.74, **0.93**, 1.18	0.75, **0.88**, 0.96
v2	0.94, **1.00**, 1.07	0.98, **0.99**, 1.00	0.74, **0.89**, 1.10	0.79, **0.89**, 0.96

zero below 1800 m [see Fig. 15(a)], and much smaller above this level than the v1 bias which was growing quite rapidly. Furthermore, the temperature RMS profile is now essentially below 1 K over the lowest 3 km for v2, whereas v1 had RMS values above 1.5 K from 700 to 2000 m. However, there was little change in the accuracy of the retrieved temperature profile at the Amazon site, with the bias and RMS profiles there remaining largely unchanged between v1 and v2, although the points on the Taylor plot were slightly more clustered for temperature at the Amazon site.

As suggested by the previous results, the water vapor bias and standard deviation profiles [see Fig. 15(b)] are largely unchanged relative to v1 [see Fig. 14(b)] at the SGP and Oliktok sites. However, the humidity bias in the Amazon data has become positive instead of negative in the lowest 1 km, is markedly smaller above 1.5 km, and is much more constant with height. Furthermore, the humidity RMS profile for the Amazon site has decreased 20% or more with the new version of the algorithm. At all sites the vertical structure of the retrieved profiles is markedly better, as shown by the reduced visual spread in the *cc* and *rs* coefficients [see Fig. 15(c) and (d) versus Fig. 14(c)

and (d)], the reduction of their interquartile range (see Table III), and their propagation towards their ideal values of (1, 1).

V. CONCLUSION AND FUTURE WORK

This paper describes the continued evolution of the AERIoe thermodynamic retrieval algorithm so that more accurate profiles can be retrieved from the downwelling infrared radiance spectra observed by the AERI. In particular, the main changes discussed here are constraints to the derived RH and potential temperature profile when the retrieval is iterating, and the incorporation of new datasets into the observation vector used by the retrieval. Both of these changes markedly improve the accuracy of the temperature profile in all environments from the tropics to the Arctic. Including the 2-channel MWR data in the retrieval produces a slight improvement in the retrieved water vapor profile, especially in the 2–4 km region, whereas including the Raman lidar data greatly improves the accuracy of the water vapor profile. These results agree with similar statistics comparing v2 retrievals with radiosondes in other mid-latitude locations, such as in southwestern Germany [40], Ellis, Kansas

and Boulder, Colorado [65], and Norman, Oklahoma [6]. Furthermore, the convective indices such as convective available potential energy, convective inhibition, and lifted index derived from AERIoe (v2) baseline retrievals showed good agreement with collocated radiosondes [66].

The accuracy of these AERIoe-retrieved profiles is approaching the requirements set forth in the various National Research Council reports [3], [4]. Given that the AERI is a commercially available instrument and AERIoe can be run in real time, AERIs could be deployed as part of a ground-based profiling network. However, as some applications will require more accurate water vapor profiles than can be currently retrieved using the v2 baseline configuration, there may be a desire to deploy a water vapor lidar alongside the AERI. Raman lidars are still research-grade instruments, but recent progress towards developing small water vapor differential absorption lidars (DIALs) that use commercially available diode-based laser sources (e.g., [62]) has been made. Work is currently underway to evaluate the impact of water vapor DIAL observations on the AERIoe retrieval, as well as to combine observations from so-called profiling MWRs (i.e., systems that make radiance observations at multiple frequencies on the side of water vapor and oxygen absorption lines) (e.g., [35] and [67]) into AERIoe using observations from the Perdigao field campaign [68].

The AERIoe framework allows a wide range of different observation types to be incorporated easily into the retrieval in the future, such as bending angle from radio occultation measurements or geostationary satellite radiances. In the latter, only channels that are insensitive to the Earth's surface should be used, unless the state vector is updated to include other important variables such as skin temperature and surface emissivity. We are currently working on evaluating and improving the spectroscopy of the 6.7 μm water vapor band so that data from this spectral region can be used in the retrievals without causing biases (as is currently the case now). Future work will investigate incorporating these and other observations into the retrieval, expand the algorithm's capability to simultaneously retrieve trace gas profiles, and assimilate these thermodynamic profile retrievals into NWP models to demonstrate their impact on difficult forecast problems such as nocturnal convection.

REFERENCES

[1] T. M. Weckwerth, V. Wulfmeyer, R. M. Wakimoto, R. M. Hardesty, J. W. Wilson, and R. M. Banta, "NCAR-NOAA lower-tropospheric water vapor workshop," *Bull. Amer. Meteorol. Soc.*, vol. 80, pp. 2339–2357, 1999.

[2] W. F. Dabberdt *et al.*, "Multifuction mesoscale observing networks," *Bull. Amer. Meteorol. Soc.*, vol. 86, pp. 961–982, 2005, doi:10.1175/BAMS-86-7-961.

[3] National Research Council (NRC), "Committee on developing mesoscale meteorological observational capabilities to meet multiple national needs," in *Observing Weather and Climate From the Ground Up: A Nationwide Network of Networks*. Washington, DC, USA: National Academies Press, 2009, 234 pp.

[4] National Research Council (NRC), "Committee on progress and priorities of U.S. weather research and research-to-operations activities," in *When Weather Matters: Science and Service to Meet Critical Societal Needs*. Washington, DC, USA: National Academies Press, 182 pp.

[5] R. M. Hoff and R. M. Hardesty, "Thermodynamic profiling technologies workshop report to the national science foundation and the national weather service," Nat. Center Atmospheric Res., Boulder, CO, USA, Tech. Note NCAR/TN-4881STR, 2012. [Online] Available: http://nldr.library.ucar.edu/repository/collections/TECH-NOTE-000-000-000-853

[6] V. Wulfmeyer *et al.*, "A review of the remote sensing of lower-tropospheric thermodynamic profiles and its indispensible role for the understanding and simulation of water and energy cycles," *Rev. Geophys.*, vol. 53, pp. 819–895, 2015, doi:10.1002/2014RG000476.

[7] G. G. Mace, T. P. Ackerman, P. Minnis, and D. F. Young, "Cirrus layer microphysical properties derived from surface- based millimeter radar and infrared interferometer data," *J. Geophys. Res.*, vol. 103, pp. 23 207–23 216, 1998, doi:10.1029/98JD02117.

[8] D. D. Turner, "Arctic mixed-phase cloud properties from AERI-lidar observations: Algorithm and results from SHEBA," *J. Appl. Meteorol.*, vol. 44, pp. 427–444, 2005, doi:10.1175/JAM2208.1.

[9] J. M. Comstock *et al.*, "An intercomparison of microphysical retrievals for upper tropospheric ice clouds," *Bull. Amer. Meteorol. Soc.*, vol. 88, pp. 191–204, 2007.

[10] D. D. Turner, "Improved ground-based liquid water path retrievals using a combined infrared and microwave approach," *J. Geophys. Res.*, vol. 112, no. D15, 2007, doi:10.1029/2007JD008530.

[11] D. C. Tobin *et al.*, "Downwelling spectral radiance observation at the SHEBA ice station: Water vapor continuum measurements from 17 to 26 μm," *J. Geophys. Res.*, vol. 104, pp. 2081–2092, 1999.

[12] D. D. Turner *et al.*, "The QME AERI LBLRTM: A closure experiment for downwelling high spectral resolution infrared radiance," *J. Atmos. Sci.*, vol. 61, pp. 2657–2675, 2004, doi:10.1175/JAS3300.1.

[13] D. D. Turner, "Ground-based retrievals of optical depth, effective radius, and composition of airborne mineral dust above the Sahel," *J. Geophys. Res.*, vol. 113, 2008, Art. no. D00E03, doi:10.1029/2008JD010054.

[14] L. Yurganov, W. McMillan, C. Wilson, M. Fischer, S. Biraud, and C. Sweeney, "Carbon monoxide mixing ratios over Oklahoma between 2002 and 2009 retrieved from atmospheric emitted radiance interferometer spectra," *Atmos. Meas. Techn.*, vol. 3, pp. 1319–1331, 2010, doi:10.5194/amt-3-1319-2010.

[15] D. R. Feldman, W. D. Collins, P. J. Gero, M. S. Torn, E. J. Mlawer, and T. R. Shippert, "Observational determination of surface radiative forcing by CO_2 from 2000-2010," *Nature*, vol. 519, pp. 339–343, 2015.

[16] W. F. Feltz, W. L. Smith, R. O. Knuteson, H. E. Revercomb, H. M. Woolf, and H. B. Howell, "Meteorological applications of temperature and water vapor retrievals from the ground-based Atmospheric Emitted Radiance Interferometer (AERI)," *J. Appl. Meteorol.*, vol. 37, pp. 857–875, 1998.

[17] W. L. Smith, W. F. Feltz, R. O. Knuteson, H. E. Revercomb, H. M. Woolf, and H. B. Howell, "The retrieval of planetary boundary layer structure using ground-based infrared spectral radiance measurements," *J. Atmos. Ocean. Technol.*, vol. 16, pp. 323–333, 1999.

[18] W. F. Feltz and J. R. Mecikalski, "Monitoring high-temporal-resolution convective stability indices using the ground-based atmospheric emitted radiance interferometer (AERI) during the 3 may 1999 Oklahoma-Kansas tornado outbreak," *Weather Forecasting*, vol. 17, pp. 445–455, 2002.

[19] W. F. Feltz, W. L. Smith, H. B. Howell, R. O. Knuteson, H. Woolf, and H. E. Revercomb, "Near-continuous profiling of temperature, moisture, and atmospheric stability using the Atmospheric Emitted Radiance Interferometer (AERI)," *J. Appl. Meteorol.*, vol. 42, pp. 584–597, 2003.

[20] T. J. Wagner, W. F. Feltz, and S. A. Ackerman, "The temporal evolution of convective indices in storm-producing environments," *Weather Forecasting*, vol. 23, pp. 786–794, 2008.

[21] D. D. Turner and U. Löhnert, "Information content and uncertainties in thermodynamic profiles and liquid cloud properties retrieved from the ground-based atmospheric emitted radiance interferometer (AERI)," *J. Appl. Meteorol. Climatol.*, vol. 53, pp. 752–771, 2014, doi:10.1175/JAM-C-D-13-0126.1.

[22] D. D. Turner and R. G. Ellingson, Eds., *The Atmospheric Radiation Measurement (ARM) Program: The First 20 Years* (Meteorol. Monograph 57). Boston, MA, USA: Amer. Meteorol. Soc., 2016.

[23] D. L Sisterson, R. A. Peppler, T. S. Cress, P. J. Lamb, and D. D. Turner, "The ARM southern great plains (SGP) site," in *The Atmospheric Radiation Measurement Program: The First 20 Years* (Meteorol. Monograph 57), Boston, MA, USA: Amer. Meteorol. Soc., 2016, pp. 6.1–6.14, doi:10.1175/AMSMONOGRAPHS-D-16-0004.1.

[24] M. A. Miller, K. Nitschke, T. P Ackerman, W. R. Ferrell, N. Hickmon, and M. Ivey, "The ARM mobile facilities," in *The Atmospheric Radiation Measurement Program: The First 20 Years* (Meteorol. Monograph 57), vol. 9. Boston, MA, USA: Amer. Meteorol. Soc., 2016, pp. 1–9, doi:10.1175/AMSMONOGRAPHS-D-15-0051.1.

[25] D. D. Turner, E. J. Mlawer, and H. E. Revercomb, "Water vapor observations in the ARM program," *The Atmospheric Radiation Measurement Program: The First 20 Years*. (Meteorol. Monograph 57), vol. 13. Boston, MA, USA: Amer. Meteorol. Soc., 2016, pp. 1–13, doi:10.1175/AMSMONOGRAPHS-D-15-0025.1.

[26] R. O. Knuteson *et al.*, "Atmospheric emitted radiance interferometer. Part I: Instrument design," *J. Atmos. Oceanic Technol.*, vol. 21, pp. 1763–1776, 2004.

[27] E. J. Mlawer and D. D. Turner, "Spectral radiation measurements and analysis in the ARM program," *The Atmospheric Radiation Measurement Program: The First 20 Years* (Meteorol. Monograph 57), vol. 14. Boston, MA, USA: Amer. Meteorol. Soc., 2016, pp. 1–14, doi:10.1175/AMSMONOGRAPHS-D-15-0027.1.

[28] E. J. Mlawer, M. J. Iacono, R. Pincus, H. W. Barker, L. Oreopoulos, and D. L. Mitchell, "Contributions of the ARM program to radiative transfer modeling for climate and weather applications," *The Atmospheric Radiation Measurement Program: The First 20 Years* (Meteorol. Monograph 57). Boston, MA, USA: Amer. Meteorol. Soc., 2016, pp. 15.1–15.19, doi:10.1175/AMSMONOGRAPHS-D-15-0041.1.

[29] R. O. Knuteson *et al.*, "Atmospheric emitted radiance interferometer. Part II: Instrument performance," *J. Atmos. Ocean. Technol.*, vol. 21, pp. 1777–1789, 2004.

[30] D. D. Turner, R. O. Knuteson, H. E. Revercomb, C. Lo, and R. G. Dedecker, "Noise reduction of atmospheric emitted radiance interferometer (AERI) observations using principal component analysis," *J. Atmos. Ocean. Technol.*, vol. 23, pp. 1223–1238, 2006.

[31] D. D. Turner, B. M. Lesht, S. A. Clough, J. C. Liljegren, H. E. Revercomb, and D. C. Tobin, "Dry bias and variability in vaisala radiosondes: The ARM experience," *J. Atmos. Ocean. Technol.*, vol. 20, pp. 117–132, 2003.

[32] J. Wang, H. L. Cole, D. J. Carlson, E. R. Miller, and K. Beirle, "Corrections of humidity measurement errors from the Vaisala RS80 radiosonde–application to TOGA COARE data," *J. Atmos. Ocean. Technol.*, vol. 19, pp. 981–1002, 2002.

[33] J. Verlinde, B. D. Zak, M. D. Shupe, M. D. Ivey, and K. Stamnes,: "The ARM north slope of alaska (NSA) sites," *The Atmospheric Radiation Measurement Program: The First 20 Years* (Meteorol. Monograph 57). Boston, MA, USA: Amer. Meteorol. Soc., 2016, pp. 8.1–8.13, doi:10.1175/AMSMONOGRAPHS-D-15-0023.1.

[34] S. T. Martin *et al.*, "The green ocean amazon experiment (GOAMAZON2014/5) observes pollution affecting gases, aerosols, clouds, and rainfall over the rain forest," *Bull. Amer. Meteor. Soc.*, vol. 98, pp. 981–998, 2017, doi:10.1175/BAMS-D-15-00221.1.

[35] F. Solheim *et al.*, "Radiometric profiling of temperature, water vapor, and cloud liquid water using various inversion methods," *Radio Sci.*, vol. 33, pp. 393–404, 1998.

[36] S. G. Benjamin *et al.*, "A north american hourly assimilation and model forecast cycle: The rapid refresh," *Monthly Weather Rev.*, vol. 144, pp. 1669–1694, 2016, doi:10.1175/MWR-D-15-0242.1.

[37] T. J. Hewison, "1D-VAR retrieval of temperature and humidity profiles from a ground-based microwave radiometer," *IEEE Trans. Geosci. Remote Sens.*, vol. 45, no. 7, pp. 2163–2168, Jul. 2007, doi:10.1109/TGRS.2007.898091.

[38] U. Löhnert and O. Maier, "Operational profiling of temperature using ground-based microwave radiometry at Payerne: Prospects and challenges," *Atmos. Meas. Techn.*, vol. 5, pp. 1121–1134, 2012, doi:10.5194/amt-5-1121-2012.

[39] U. Löhnert, D. D. Turner, and S. Crewell, "Ground-based temperature and humidity profiling using spectral infrared and microwave observations. Part 1: Simulated retrieval performance in clear sky conditions," *J. Appl. Meteorol. Climatol.*, vol. 48, pp. 1017–1032, 2009, doi:10.1175/2008JAMC2060.1.

[40] W. G. Blumberg, D. D. Tuner, U Löhnert, and S. Castleberry, "Ground based temperature and humidity profiling using spectral infrared and microwave observations. Part II: Actual retrieval performance in clear-sky and cloudy conditions," *J. Appl. Meteorol. Climatol.*, vol. 54, pp. 2305–2319, 2015.

[41] M. P. Cadeddu, J. C. Liljegren, and D. D. Turner, "The atmospheric radiation measurement (ARM) program network of microwave radiometers: Instruments, data, and retrievals," *Atmos. Meas. Tech.*, vol. 6, pp. 2359–2372, 2013, doi:10.5194/amt-6-2359-2013.

[42] D. D. Turner, S. A. Clough, J. C. Liljegren, E. E. Clothiaux, K. Cady-Pereira, and K. L. Gaustad, "Retrieving liquid water path and precipitable water vapor from atmospheric radiation measurement (ARM) microwave radiometers," *IEEE Trans. Geosci. Remote Sens.*, vol. 45, no. 11, pp. 3680–3690, Nov. 2007, doi:10.1109/TGRS.2007.903703.

[43] D. D. Turner, J. E. M. Goldsmith, and R. A. Ferrare, "Development and applications of the ARM Raman lidar," *The Atmospheric Radiation Measurement Program: The First 20 Years* (Meteorol. Monograph 57). Boston, MA, USA: Amer. Meteorol. Soc., 2016, pp. 18.1–18.15, doi:10.1175/AMSMONOGRAPHS-D-15-0026.1.

[44] J. E. M. Goldsmith, F. H. Blair, S. E. Bisson, and D. D. Turner, "Turn-key raman lidar for profiling atmospheric water vapor, clouds, and aerosols," *Appl. Opt.*, vol. 37, pp. 4979–4990, 1998.

[45] R. K. Newsom, D. D. Turner, B. Mielke, M. Clayton, R. Ferrare, and C. Sivaraman, "The use of simultaneous analog and photon counting detection for raman lidar," *Appl. Opt.* vol. 48, pp. 3903–3914, 2009, doi:10.1364/AO.48.003903.

[46] D. D. Turner and J. E. M. Goldsmith, "Twenty-four-hour raman lidar water vapor measurements during the atmospheric radiation measurement program's 1996 and 1997 water vapor intensive observation periods," *J. Atmos. Ocean. Technol.* vol. 16, pp. 1062–1076, 1999.

[47] D. D. Turner, V. Wulfmeyer, L. K. Berg, and J. H. Schween, "Water vapor turbulence profiles in stationary continental convective mixed layers," *J. Geophys. Res.* vol. 119, pp. 1–15, 2014, doi:10.1002/2014JD022202.

[48] C. D Rodgers, *Inverse Methods for Atmospheric Sounding: Theory and Practice* (Series on Atmospheric, Oceanic, and Planetary Physics), vol. 2. Singapore: World Scientific, 2000, 238 pp.

[49] D. D. Turner and E. W. Eloranta, "Validating mixed-phase cloud optical depth retrieved from infrared observations with high spectral resolution lidar," *IEEE Geosci. Remote Sens. Lett.*, vol. 5, no. 2, pp. 285–288, Apr. 2008, doi:10.1109/LGRS.2008.915940.

[50] K. Khosravian, "CO_2 profiling in the lower troposphere using a high spectral resolution infrared radiometer," Ph.D. dissertation, Univ. Cologne, Cologne, Germany, 2017.

[51] E. J. Mlawer, V. H. Payne, J.-L. Moncet, J. S. Delamere, M. J. Alvarado, and D. C. Tobin, "Development and recent evaluation of the MT_CKD model of continuum absorption," *Phil. Trans. R. Soc. A.*, vol. 370, pp. 2520–2556, 2012, doi:10.1098/rsta.2011.0295.

[52] S. A. Clough *et al.*, "Atmospheric radiative transfer modeling: A summary of the AER codes," *J. Quantitative Spectroscopy Radiative Transfer*, vol. 91, pp. 233–244, 2005, doi:10.1016/j.jqsrt.2004.05.058.

[53] T. J. Wagner, P. M. Klein, and D. D. Turner, "A new generation of ground-based mobile platforms for active and passive profiling of the boundary layer," *Bull. Amer. Meteorol. Soc.*, to be published.

[54] A. Carissimo, I. De Feis, and C. Serio, "The physical retrieval methodology for IASI: The ∂-IASI code," *Environ. Model. Softw.*, vol. 20, pp. 1111–1126, 2005, doi:10.1016/j.envsoft.2004.07.003.

[55] G. Masiello, C. Serio, and P. Antonelli, "Inversion for atmospheric thermodynamic parameters of IASA data in the principal components space," *Quart. J. Roy. Meteorol. Soc.*, vol. 138, pp. 103–117, 2012.

[56] B. Geerts *et al.*, "The 2015 plains elevated convection at night field project," *Bull. Amer. Meteorol. Soc.*, vol. 98, pp. 767–786, 2017.

[57] V. H. Payne, E. J. Mlawer, K. E. Cady-Pereira, and J.-L. Moncet, "Water vapor continuum absorption in the microwave," *IEEE Trans. Geosci. Remote Sens.*, vol. 49, no. 6, pp. 2194–2208, Jun. 2011, doi:10.1109/TGRS.2010.2091416.

[58] D. D. Turner, U. Löhnert, M. Cadeddu, S. Crewell, and A. Vogelmann, "Modifications to the water vapor continuum in the microwave suggested by ground-based 150 GHz observations," *IEEE Trans. Geosci. Remote Sens.*, vol. 47, no. 10, pp. 3326–3337, Oct. 2009, doi:10.1109/TGRS.2009.202262.

[59] S.-A. Boukabara, S. A. Clough, J.-L. Moncet, A. F. Krupnov, M. Y. Tretyakov, and V. V. Parshin, "Uncertainties in the temperature dependence of the line-coupling parameters of the microwave oxygen band: Impact study," *IEEE Trans. Geosci. Remote Sens.*, vol. 43, no. 5, pp. 1109–1114, May 2005, doi:10.1109/TGRS.2004.839654.

[60] M. P. Cadeddu, V. H. Payne, S. A. Clough, K. Cady-Pereira, and J. C. Liljegren, "Effect of the oxygen line-parameter modeling on temperature and humidity retrievals from ground-based microwave radiometers," *IEEE Trans Geosci. Remote Sens.*, vol. 45, no. 7, pp. 2216–2223, Jul. 2007, doi:10.1109/TGRS.2007.894063.

[61] D. D. Turner, S. Kneifel, and M. P. Cadeddu, "An improved liquid water absorption model at microwave frequencies for supercooled liquid water clouds," *J. Atmos. Ocean. Technol.*, vol. 33, pp. 33–44, 2016, doi:10.1175/JTECH-D-15-0074.1.

[62] S. M. Spuler, K. S. Repasky, B. Morley, D. Moen, M. Hayman, and A. R. Nehrir, "Field-deployable diode-laser-based differential absorption lidar (DIAL) for profiling water vapor," *Atmos. Meas. Techn.* vol. 8, pp. 1073–1087, 2015, doi:10.5194/AMT-8-1073-2015.

[63] M. Barrera-Verdejo, S. Crewell, U. Löhnert, E. Orlandi, and P. Di Girolamo, "Ground-based lidar and microwave radiometry synergy for high vertical resolution absolute humidity profiling," *Atmos. Meas. Techn.*, vol. 9, pp. 4013–4028, 2016, doi:10.5194/amt-9-4013-2016.

[64] P. Klein *et al.*, "LABLE: A multi-institutional, student-led, atmospheric boundary layer experiment," *Bull. Amer. Meteorol. Soc.*, vol. 96, pp. 1743–1764, 2015, doi:10.1175/BAMS-D-13-00267.1.

[65] T. M. Weckwerth, K. Weber, D. D. Turner, and S. M. Spuler, "Validation of a new water vapor micropulse differential absorption lidar (DIAL)," *J. Atmos. Ocean. Technol.*, vol. 33, pp. 2353–2372, 2016, doi:10.1175/JTECH-D-16-0119.1.

[66] W. G. Blumberg, T. J. Wagner, D. D. Turner, and J. Correia Jr., "Quantifying the accuracy and uncertainty of diurnal thermodynamic profiles and convection indices derived from the atmospheric emitted radiance interferometer," *J. Appl. Meteorol. Climatol.*, vol. 56, pp. 2747–2766, 2017, doi:10.1175/JAMC-D-17-0036.1.

[67] T. Rose, S. Crewell, U. Löhnert, and C. Simmer, "A network suitable microwave radiometer for operational monitoring of the cloudy atmosphere," *Atmos. Res.*, vol. 75, pp. 183–200, 2005, doi:10.1016/j.atmosres.2004.12.005.

[68] H. J. Fernando *et al.*, "The Perdigao: Peering into microscale details of mountain winds," *Bull. Amer. Meteorol. Soc.*, accepted for publication.

David D. Turner received the B.A. and M.S. degrees in mathematics from Eastern Washington University, Cheney, WA, USA, in 1992 and 1994, respectively, and the Ph.D. degree in atmospheric science from the University of Wisconsin–Madison, Madison, WI, USA, in 2003.

He is currently a Physical Meteorologist with the Global Systems Division, Earth System Research Laboratory, National Oceanic and Atmospheric Administration, Boulder, CO, USA. His research interests include infrared and microwave remote sensing, radiative transfer in clear and cloudy atmospheres, water vapor and wind profiling lidar technologies, retrieval theory, and using these observations to improve our ability to model the evolution of the atmospheric boundary layer over the diurnal cycle an during dynamic weather events.

Dr. Turner is a member of the American Meteorological Society and the American Geophysical Union.

William G. Blumberg (Greg) received the B.A., M.S., and Ph.D. degrees in meteorology from the University of Oklahoma, Norman, OK, USA, in 2011, 2013, and 2018, respectively.

During his graduate studies, he was with the Cooperative Institute for Mesoscale Meteorological Studies (CIMMS). His research interests include the diurnal evolution of the boundary layer, forecasting, severe weather, meteorological education, and psychology of weather. He is a developer of SHARPpy, an internationally used, open-source sounding analysis program.

Dr. Blumberg is a member of the American Meteorological Society and regularly teaches and mentors undergraduates and high-school students.